Desalination and Water Treatment
www.deswater.com

doi: 10.5004/dwt.2023.29743

302 (2023) 104–120
August

Removal of fluoride by biochar from watermelon rind – an efficient application in groundwater treatment

Qi Sha[a], Huidong Xie[a,*], Zhirui Zhang[a], Chang Yang[b], Ruxia Zhao[c], Chengmin Ge[d]

[a]*School of Chemistry and Chemical Engineering, Xi'an University of Architecture and Technology, Xi'an 710055, Shaanxi, China, emails: xiehuidong@tsinghua.org.cn (H.D. Xie), 1324534889@qq.com (Q. Sha), 962285999@qq.com (Z.R. Zhang)*
[b]*Division of Laboratory and Equipment Management, Xi'an University of Architecture and Technology, Xi'an 710055, Shaanxi, China, email: 1059890481@qq.com*
[c]*Shandong Drug and Food Vocational College, Weihai 264210, Shandong, China, email: 363669481@qq.com*
[d]*Shandong Dongyuan New Material Technology Co., Ltd., Dongying 257300, Shandong, China, email: gechengmin@163.com*

Received 17 December 2022; Accepted 28 June 2023

ABSTRACT

Fluoride pollution in groundwater is mainly from natural factors, which will harm those who use groundwater as drinking water. Herein, an iron-lanthanum watermelon rind biochar composite was prepared by a coprecipitation method and used to remove fluoride from the aqueous solution by a static adsorption method. The effects of adsorbent composition, aging time, calcination temperature, pH, adsorption time, adsorbent dosage, adsorption temperature, initial concentration of fluoride, and coexisting anions on the removal of fluoride were evaluated. When the amount of adsorbent was 0.05 g/50 mL, the removal efficiency of the fluoride with an initial concentration of 10 mg/L reached 98.29%. The best conditions for the static adsorption process of 10 mg/L fluoride were: pH was in the range 2–9, the amount of adsorbent was 0.05 g/50 mL, and the reaction time was 5 h. Scanning electron microscopy-energy-dispersive X-ray spectroscopy, Fourier-transform infrared spectroscopy, X-ray diffraction, X-ray photoelectron spectroscopy, and Brunauer–Emmett–Teller of the adsorbent were tested. Experimental results showed that electrostatic attraction, metal complexation, and ion exchange were the main adsorption mechanisms. The calculated value of k_2 varies from 0.2943 to 0.0071 g/mg·min with the decrease of the fluoride concentration. The kinetics and isotherm showed that chemical adsorption was the main control step in the fluoride adsorption of Fe-La-WBC-300. The value of the Freundlich constant (n) in the range 0–1 showed that Fe-La-WBC-300 had the best performance for fluoride removal. The fluoride adsorption process consisted of single-layer adsorption and multilayer adsorption. Thermodynamic studies showed that the adsorption of fluoride was a process of spontaneous endothermic reaction. Fe-La-WBC-300 showed a good application prospect to remove fluoride in groundwater.

Keywords: Fluoride; Biochar; Adsorption; Groundwater; Watermelon rind

1. Introduction

As an evaluation of drinking water quality, fluoride plays a very important role in human health. A proper amount of fluoride is beneficial to human bone development and dental health, but excessive fluoride can cause harm to human health, such as endocrine gland disease, cardiovascular disease, gastrointestinal irritation, neurological disease, cancer, osteoporosis, etc. It is reported that the fluoride concentration in drinking water is beneficial to the human body when the concentration of fluoride is in the range of 0.5–1.5 mg/L [1–4]. Fluorine pollution will also cause harm

* Corresponding author.

to air, water ecology, and soil ecological environment, thus the growth of animals, plants, and crops is destroyed [5–9]. In some rural areas of developing countries, groundwater is the main source of drinking water. Due to the widespread presence of fluoride in nature, the fluoride content in some groundwater exceeds the drinking water standard limit [10,11]. In addition, the excessive fluorine-containing industrial wastewater discharged from the factory contributes also another reason for fluoride pollution of groundwater [12]. Therefore, more and more researchers focus on solving the problem of fluoride pollution.

Currently, the methods to remove fluoride pollution in water bodies mainly include: adsorption [13], precipitation [14], ion-exchange [15], reverse osmosis [16], nanofiltration [17], and electrodialysis [18]. Among these technologies, adsorption is a method that usually uses natural or synthetic solid adsorbents to remove fluoride in polluted water. Owing to the advantages of high economic value, high removal efficiency, simple operation, strong pertinence, etc. the adsorption methods are favored by researchers [19]. Biomass charcoal made from agricultural or food waste or other by-products was extensively used to adsorb and remove fluoride in water because of the large surface area, high availability of materials, and good economic benefits [20]. For example, Wan et al. [21] reported a simple one-step pyrolysis process to obtain a mixed adsorbent MgO-BC by impregnating magnesium oxide into biochar. Mei et al. [22] prepared zirconium dioxide-biochar (ZrO_2/BC) via one-step calcination of zirconium-impregnated *Camellia oleifera* seed shells. Both MgO-BC and ZrO_2/BC showed high defluorinating efficiency. Meilani et al. [23] prepared the aluminum-impregnated biochar extracted from food waste (Al-FWB), which showed a maximum adsorption capacity of 123.4 mg/g. In addition to the above materials, rare earth metal oxides are also used in the removal of fluoride ions and other anions because of their high adsorption capacity [24].

At present, the biomass charcoal materials reported to adsorb and remove fluoride include banana peels [25], peanut shells [26], rice husks [27], corn cob [22], tea leaves [28], etc. Among them, watermelon rind is rich in carbohydrates, phenolic compounds, and fatty acids. The carbohydrate contained is mainly composed of cellulose, hemicellulose, and pectin. Therefore, watermelon rind is very suitable for the preparation of biochar [29–31]. However, the fluoride adsorption of the biochar is greatly affected by the pH of the solution if used alone. Sadhu et al. [32] used watermelon rind biochar to remove fluoride, which showed a maximum adsorption capacity of 9.5 mg/g at pH = 1. Because the actual groundwater is generally close to a neutral environment, it is necessary to develop a new absorbent which shows good adsorption in the neutral environment. It has been reported that lanthanum hydroxide and iron oxide have good adsorption properties for fluoride. Wang et al. [33] prepared lanthanum-modified pomelo peel biochar, which showed a maximum adsorption capacity of 19.86 mg/g. Dewage et al. [34] prepared biochar composite with high surface area by dispersing α-Fe_2O_3 and Fe_3O_4 on Douglas Fir, which could quickly remove nitrate and fluoride ions from water and easily be separated by using magnetic technology. Therefore, Fe-La-loaded watermelon rind biochar may become a new adsorbent to remove fluoride. As far as we know, there are no reports on the removal of fluoride by Fe-La-loaded watermelon rind biochar in the literature.

In this present work, watermelon rind biochar loaded with iron and lanthanum was prepared by a coprecipitation method. The ability to remove fluoride from the aqueous solution was evaluated by a static adsorption method. The effects of different experimental conditions on the adsorption effect of fluoride were explored, and the adsorption mechanism was analyzed.

2. Materials and methods

2.1. Chemicals and reagents

All chemicals, including sodium fluoride, sodium citrate dihydrate, sodium nitrate, hydrochloric acid, sodium hydroxide, iron trichloride, and lanthanum nitrate hexahydrate were of analytical grade with no further purification. A 100 mg/L fluoride standard solution was prepared by dissolving 0.2210 g sodium fluoride in 1.0 L deionized water, and other concentrations of fluoride were obtained by diluting the original solution. The total ionic strength was adjusted by buffer solution prepared according to the method in GB 7484-87. The pH of the fluoride solution was adjusted by using 0.1 M HCl and 0.1 M NaOH solutions and measured by a pH meter. The manufacturing company and purity of the experimental chemical reagents are shown in Table 1.

2.2. Preparation of the biosorbent

The watermelon rind was collected on the campus. First, the watermelon flesh part was removed and washed three times with deionized water and then dried in an oven at

Table 1
Manufacturing company and purity of the experimental chemical reagents

Chemical reagent	Purity	Manufacturing company
NaF	AR	Tianjin Dongli District Tianda Chemical Reagent Factory (Tianjin, China)
$C_6H_5Na_3O_7{\cdot}2H_2O$	AR	Sinopharm Chemical Reagent Co., Ltd., (China)
$NaNO_3$	AR	Sinopharm Chemical Reagent Co., Ltd., (China)
HCl	AR	Xi'an Chemical Reagent Factory, (China)
NaOH	AR	Xi'an Chemical Reagent Factory, (China)
$FeCl_3$	AR	Tianjin Kemiou Chemical Reagent Co., Ltd., (Tianjin, China)
$La(NO_3)_3{\cdot}6H_2O$	AR	Adamas Reagent Co., Ltd., (China)

80°C for 48 h. After that, the watermelon rinds were ground and passed through a 100-mesh sieve, then stored in a sealed container. Next, 10 g powder was weighed and heated in a tube furnace at 300°C for 2 h under an N_2 atmosphere with a heating rate of 5°C/min. The obtained watermelon rind biochar sample was denoted as WBC-300. Similarly, WBC-600 meant the samples calcinated at 600°C under the same conditions. For the preparation of Fe-La loaded watermelon rind biochar, 1.2166 g $FeCl_3$ and 3.2475 g·$La(NO_3)_3 \cdot 6H_2O$ were added to a beaker containing 30 mL water and 10 mL ethanol and stirred for 30 min. Then, 0.5 g WBC-300/WBC-600 was added and stirred for 60 min. Then, 2 mol/L NaOH was dripped until the pH reached 8.5 and the suspension was stirred for 24 h at room temperature. The suspension was aged for 4/6/8/24 h at 60°C in an oven and then filtered and washed several times with deionized water. Finally, the sample was dried at 60°C for 24 h and labelled as Fe-La-WBC-300 and Fe-La-WBC-600. For comparison, similar conditions were used to prepare Fe-loaded adsorbent labelled as Fe-WBC-300.

2.3. Characterization

X-ray diffraction (XRD) pattern (Bruker D8, Germany) was used to observe the phase of the adsorbent by an X-ray diffractometer equipped with Cu-Kα radiation. A field-emission scanning electron microscopy (FE-SEM, GeminiSEM 500, Zeiss, Germany) combined with an energy-dispersive X-ray spectrometer (EDS) was used to observe the morphology and elemental composition. A Fourier-transform infrared spectrometer (FTIR, Nicolet iS50, Thermo Fisher Scientific, America) was used to measure the functional groups of the adsorbent. An X-ray photoelectron spectrometer (XPS, Thermo ESCALAB 250Xi, America) was used to observe the atomic valence changes of the adsorbent, in which the binding energy 284.6 eV of C 1s was used as the binding energy calibration and argon ion was used to etch the samples. An automatic specific surface and porosity analyzer (Mike ASAP 2460) was used to obtain the Brunauer–Emmett–Teller (BET) specific surface area, pore volume, pore size, and distribution of the adsorbent.

2.4. Adsorption experiments

First, 0.01–0.15 g adsorbent was added to 50 mL fluoride solution (5, 10, 20, 40, 50, 80, and 100 mg/L) in a 100 mL polyethylene conical flask at a certain temperature (298–328 K). Next, the flask oscillated in a water bath shaker (SHA-B, Hangzhou Jingfei) at a speed of 180 rpm for a certain time (10, 20, 30, 40, 50, 60, 90, 120, 150, 180, 210, 240, 300, and 360 min). After that, the mixture was filtered with a 0.45 μm filter membrane, and the unadsorbed fluoride concentration in the filtrate was measured by a fluoride ion electrode (Raymagnet PXSJ-216F, China). The influence of different raw material compositions, adsorbent aging time, calcination temperature, pH, shaking time, adsorbent dosage, adsorption temperature, and initial fluoride concentration on the fluoride adsorption will be described in detail later. Finally, the effects of coexisting anions (SO_4^{2-}, CO_3^{2-}, Cl^-, HCO_3^-, PO_4^{3-}) on the fluoride removal efficiency of Fe-La-WBC-300, the performance of adsorbent recycling, and the application effect of adsorbent in groundwater were explored. The adsorption capacity per unit mass of the adsorbent (Q_t) is calculated using Eq. (1):

$$Q_t = \frac{\left(C_0 - C_t\right) \times V}{m} \tag{1}$$

where C_0 (mg/L) is the initial concentration of fluoride, C_t (mg/L) is the concentration of fluoride at time t, V (L) is the volume of the solution, and m (g) is the mass of the adsorbent.

By replacing C_t with the concentration of fluoride at adsorption equilibrium (C_e) in Eq. (1), the equilibrium adsorption amount of fluoride Q_e (mg/g) can be calculated.

The removal efficiency of fluoride can be calculated by Eq. (2):

$$E(\%) = \frac{\left(C_0 - C_t\right)}{C_0} \times 100 \tag{2}$$

Except for studying the effect of pH on the adsorption efficiency, all experiments were performed under the pristine pH. The experimental data were fitted by the Langmuir and Freundlich isotherms to understand the adsorption process.

3. Results and discussion

3.1. SEM images and EDS

Fig. 1 shows the SEM (GeminiSEM 500) images of watermelon rind biomass, WBC-300, Fe-La-WBC-300 before and after adsorption, and EDS of Fe-La-WBC-300 before and after adsorption. The dried watermelon rind biomass in Fig. 1a shows a fibrous structure. After calcination, the pores on the surface of WBC-300 in Fig. 1b became larger. The small spherical particles in Fig. 1c might be the lanthanum oxide and iron oxide on the adsorbent, which was consistent with the literature [35]. After adsorbing fluoride, the surface of Fe-La-WBC-300 in Fig. 1d became denser. From Fig. 1e and f the characteristic peak of fluorine appeared after adsorption, which came from the adsorbed fluoride.

3.2. Fourier-transform infrared spectroscopy

Fig. 2 shows the FTIR (IRPrestige-21 FT-IR8400S) spectra of watermelon rind biomass, WBC-300, WBC-600, and Fe-La-WBC-300 before and after adsorption. The FTIR spectra of watermelon rind biomass (Curve a) show the characteristic absorption bands of polysaccharide cellulose and hemicellulose (1,000–1,200 cm^{-1}), and wide O–H bending vibration at 3,200–3,400 cm^{-1} [32]. The band at 1,053.39 cm^{-1} is attributed to the C–O and C–O–C stretching, which is characteristic of a cellulose-like structure. The peak at 1,377.96 cm^{-1} may be caused by the C–O bond in the carboxylate [32]. Compared with watermelon rind biomass, the intensity of cellulose and hemicellulose polysaccharides in WBC-300 decreased (Curve b). The O–H peak at 3,117.72 cm^{-1} in WBC-600 (Curve c) almost disappeared, and the characteristic peaks of cellulose-like structure decreased because of the high temperature. For Fe-La-WBC-300, the peak at 1,403.75 cm^{-1} may be

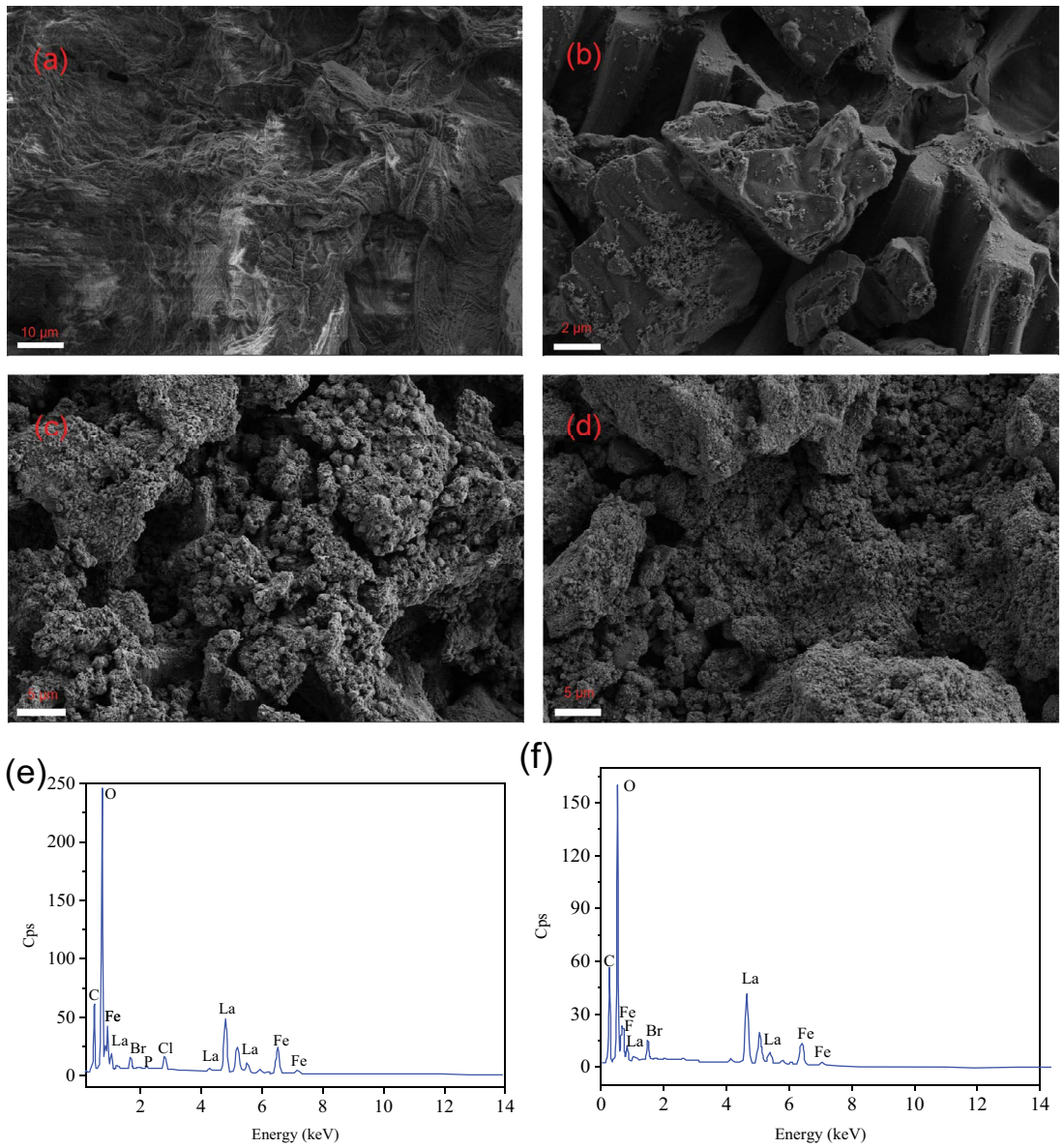

Fig. 1. Scanning electron microscopy images of (a) watermelon rind biomass, (b) WBC-300, (c) Fe-La-WBC-300 before adsorption, (d) Fe-La-WBC-300 after adsorption, (e) EDS of Fe-La-WBC-300 before adsorption and (f) EDS of Fe-La-WBC-300 after adsorption.

caused by the NO_3^- from the preparation process and the strong absorption at 644.60 cm^{-1} is due to La-OH bending vibration, as shown in Curve d [36]. After fluoride adsorption, the band at 644.60 cm^{-1} (Curve e) shifts to a higher frequency at 652.30 cm^{-1}, indicating the adsorption of fluorine [37]. The peak of 3,383.01 cm^{-1} shifts to 3,363.65 cm^{-1}, which might be due to the ion exchange between fluoride and the O–H group [38].

3.3. X-ray diffraction

Fig. 3 shows the XRD (D8) patterns of WBC-300 and Fe-La-WBC-300. The broad peak at about 22.5° and the weak broad peak at 44° of WBC-300 are caused by the (002) plane and the (100) plane of the graphite crystallites, respectively [32]. The strong sharp peaks in WBC-300 mainly correspond to potassium chloride (JCPDS: 96-900-3130) and potassium sulfate (JCPDS: 96-210-1319) [39]. The diffraction peaks of Fe-La-WBC-300 are mainly composed of FeO(OH) (JCPDS: 29-0713) and $La(OH)_3$ (JCPDS: 96-403-1382). The results prove that iron and lanthanum were loaded on the watermelon rind biochar.

3.4. X-ray photoelectron spectroscopy

Fig. 4 shows the experimental and fitted XPS (X-ray photoelectron spectroscopy, Thermo ESCALAB 250Xi) of Fe-La-WBC-300 before and after adsorption. In Fig. 4a the peak at 529.67 and 531.57 eV can be attributed to the lattice oxygen and surface adsorbed oxygen of the hydroxyl group, respectively. In Fig. 4b the –OH peak became weakened and moved to the higher energy direction after adsorption,

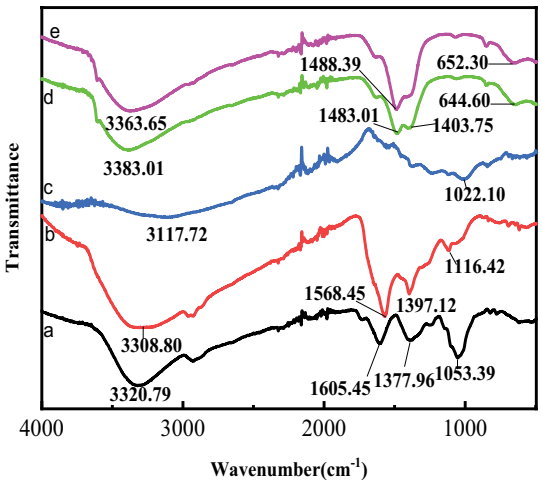

Fig. 2. Fourier-transform infrared spectra of (a) watermelon rind biomass, (b) WBC-300, (c) WBC-600, (d) Fe-La-WBC-300 before adsorption and (e) Fe-La-WBC-300 after adsorption.

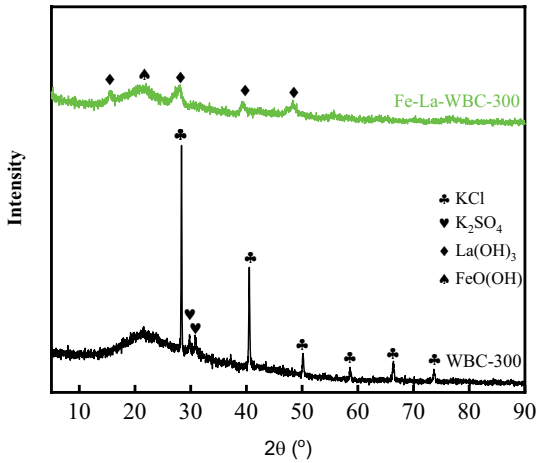

Fig. 3. X-ray diffraction pattern of the WBC-300 and Fe-La-WBC-300.

indicating that –OH was involved in fluoride adsorption [40]. Due to the charge transfer or oscillation process, the satellite peak of Fe $2p_{1/2}$ at 719 eV can also be observed, as shown in Fig. 4c and d. The peak of Fe $2p_{1/2}$ shifted to higher binding energy after adsorption, indicating that the hydroxyl group on the surface of FeOOH was replaced by fluoride [41–44]. In Fig. 4e the lanthanum spectra have two main sets of La $3d_{5/2}$ and La $3d_{3/2}$ [45]. After adsorption, all the La 3d peaks shifted to higher binding energies (from 855.87, 852.33, 839.03, 835.44 eV to 856.19, 852.77, 839.28, 835.85 eV), which may be due to the formation of lanthanum fluoride [46], as shown in Fig. 4f. In Fig. 4g no fluorine peak before adsorption was found, while the F 1s (684.97 eV) peak could be found after adsorption as shown in Fig. 4h, indicating the formation of La-F or Fe-F [47]. Since FeO(OH) and $La(OH)_3$ have ligand exchange with fluoride ions, the positively charged Fe and La can adsorb fluoride ions through electrostatic attraction [19].

3.5. N_2 adsorption and desorption

Table 2 shows the BET specific surface area, pore volume, and average pore size of Fe-La-WBC-300 measured by the N_2 adsorption–desorption isotherm. Fig. 5 shows the N_2 adsorption–desorption curves and pore volume distributions of Fe-La-WBC-300. As shown in Fig. 5a, the adsorption–desorption curve belongs to type IV, characterized by a slow increase of adsorption capacity in low-pressure range, a hysteresis loop in the medium-pressure zone, and a rapid increase of adsorption capacity in the high-pressure zone. The Barrett–Joyner–Halenda method is used to characterize the pore-size distribution of the adsorbent particles, as shown in Fig. 5b. The pore size of Fe-La-WBC-300 is concentrated in the range of 2–5 nm, which belongs to a mesoporous structure. The large specific surface area of 137.97 m^2/g and the nanoscale pore size of 2–5 nm have advantages for an adsorbent.

3.6. Effects of calcination temperature of Fe-La-WBC on the fluoride removal

Fig. 6 shows the influence of the calcination temperature of Fe-La-WBC on the fluorine removal efficiency and adsorption capacity. In the experiments, the initial fluoride concentration was 10 mg/L, the adsorption was performed at 298 K for 5 h, and the amount of the adsorbent was 0.01–0.15 g/50 mL. With the increase of the adsorbent dosage to 0.05 g, the removal efficiency and adsorption capacity of fluoride over Fe-La-WBC-300 and Fe-La-WBC-600 have almost no difference. Hereafter, Fe-La-WBC-300 was used in the subsequent experiments.

3.7. Comparison of different adsorbents on the fluoride removal

Fig. 7 shows the comparison of the fluoride removal of WBC-300, Fe-WBC-300, and Fe-La-WBC-300. In these experiments, the initial fluoride concentration was 10 mg/L, the aging time during the preparation was 4 h, the adsorption time was 5 h, and the amount of adsorbent varied in the range of 0.01–0.15 g/50 mL. As shown in Fig. 7a and b, with the increase of the adsorbent dosage, Fe-La-WBC-300 has much higher fluoride removal efficiency and adsorption capacity than WBC-300 and Fe-WBC-300. When the adsorbent added was 0.05 g/50 mL, the fluorine removal efficiency over Fe-La-WBC-300 reached up to 98.29%, and the adsorption capacity was 3.3 mg/g. Hereafter, Fe-La-WBC-300 adsorbent was used for the experimental exploration.

3.8. Effects of the oscillation time and the aging time on the fluoride removal

Fig. 8 shows the effect of aging time on the fluorine removal efficiency and adsorption capacity of Fe-La-WBC-300 under different oscillation times. The initial concentration of fluoride was 10 mg/L, the adsorption dosage was 0.05 g/50 mL, and the adsorption time was 10–360 min. As can be seen, with the prolonged adsorption time, both the adsorption efficiency and capacity increased [48]. The removal efficiency was higher than 95% and tended to stabilize at 300 min. The adsorbent prepared with an aging

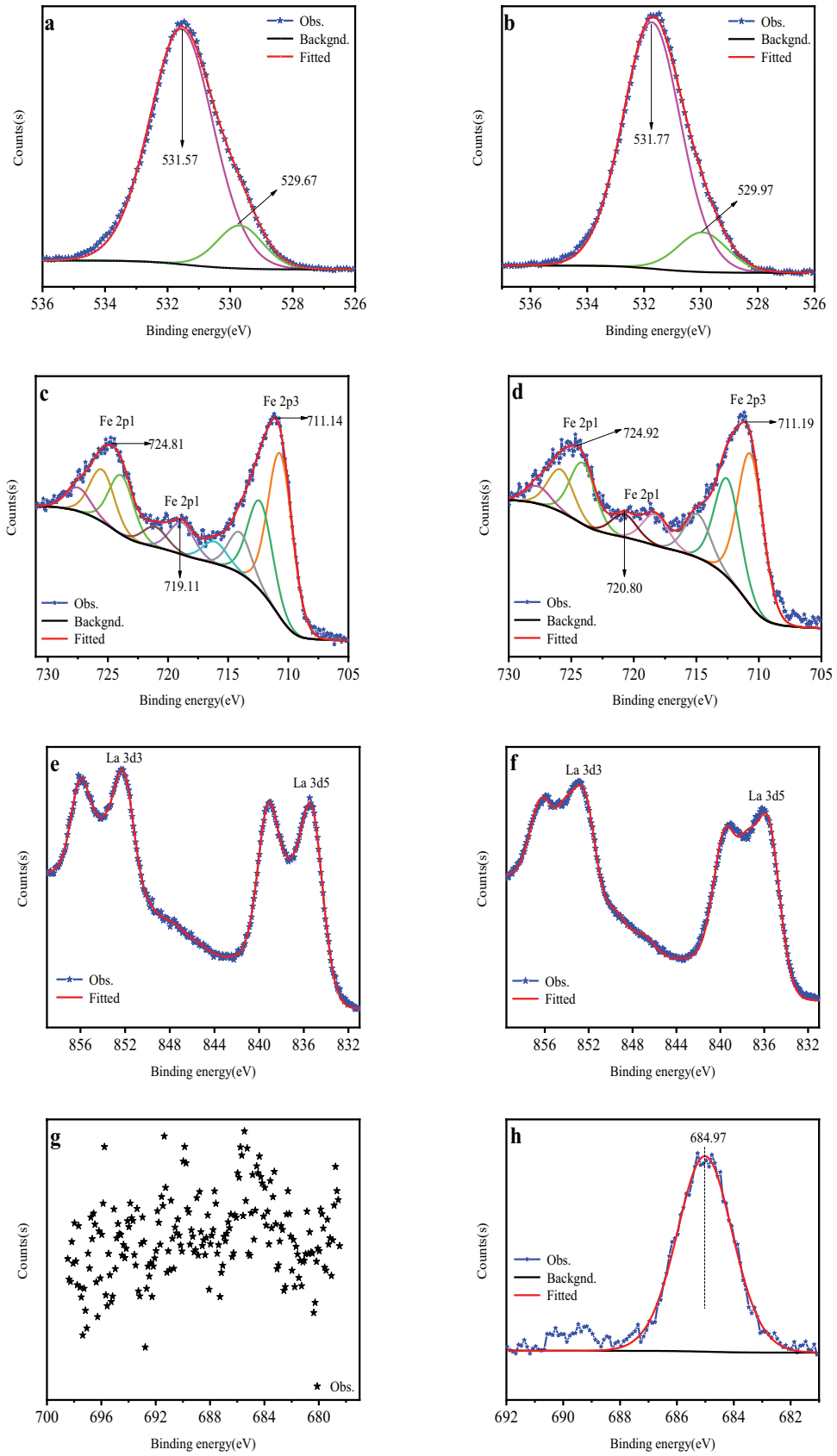

Fig. 4. X-ray photoelectron spectra of (a) O 1s before adsorption, (b) O 1s after adsorption, (c) Fe 2p before adsorption, (d) Fe 2p after adsorption, (e) La 3d before adsorption, (f) La 3d after adsorption, (g) F 1s before adsorption and (h) F 1s after adsorption.

Table 2
Brunauer–Emmett–Teller specific surface area, pore volume, and pore size of Fe-La-WBC-300

Parameters	Fe-La-WBC-300
S_{BET} (m^2/g)	137.97
Pore volume (cm^3/g)	0.1443
Average pore size (nm)	4.1341

time of 4 h showed the highest adsorption efficiency and adsorption capacity.

3.9. Effects of pH on the fluoride removal

Fig. 9 shows the removal efficiency and adsorption capacity of fluoride and the pH after adsorption varied with the pH of the solution in the range 2–12. The initial concentration of fluoride was 10 mg/L, the adsorption dosage of

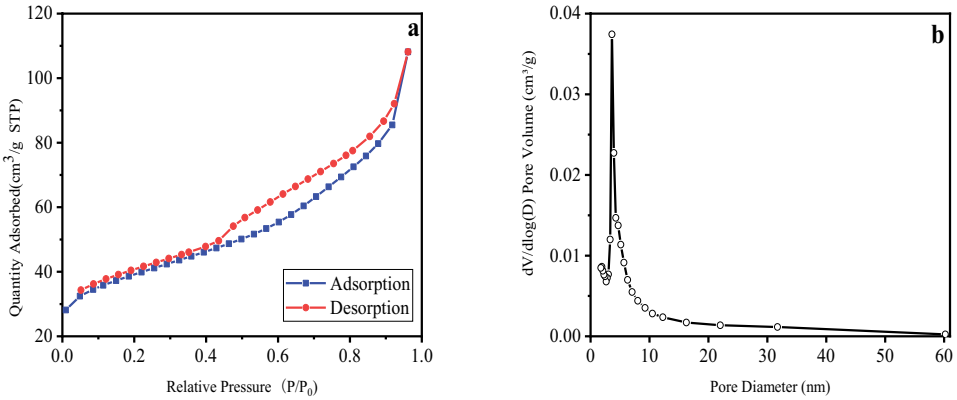

Fig. 5. (a) N_2 adsorption–desorption curves and (b) pore-size distributions of Fe-La-WBC-300. (Temp.: 77.3 K, equilibration interval: 10 s).

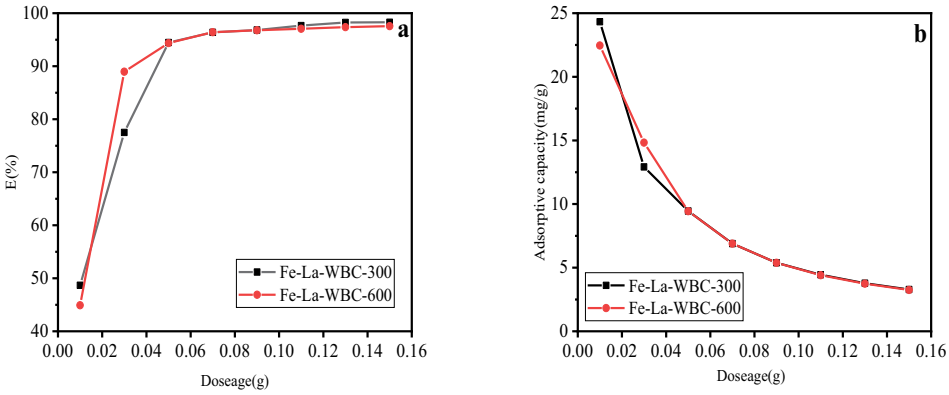

Fig. 6. Comparison of the fluoride removal between Fe-La-WBC-300 and Fe-La-WBC-600. (a) *E*(%) and (b) adsorption capacity.

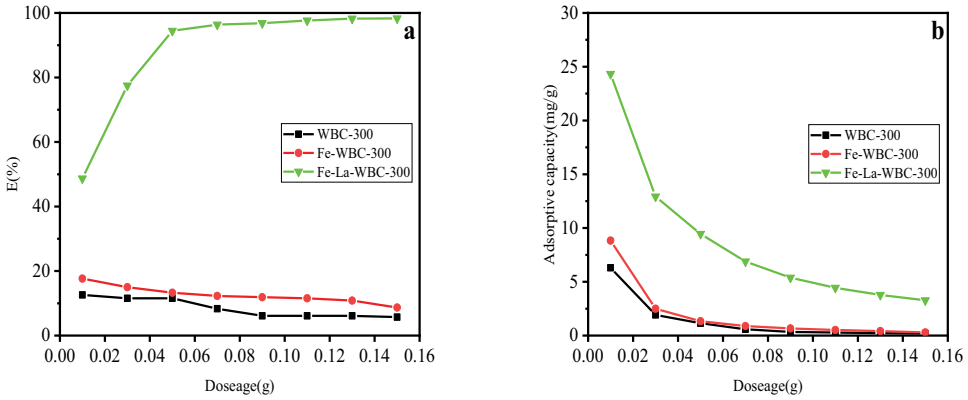

Fig. 7. Comparison of the fluoride removal of WBC-300, Fe-WBC-300 and Fe-La-WBC-300. (a) *E*(%) and (b) adsorption capacity.

Fe-La-WBC-300 was 0.05 g, and the adsorption time was 5 h. As shown in Fig. 9a, when the pH changes in the range of 2–9, the removal efficiency keeps unchanged and can exceed 94%. When the pH is greater than 9, the adsorption efficiency dropped significantly. Then the higher the pH value, the lower the adsorption efficiency. The change in adsorption capacity with pH shows a similar trend with the adsorption efficiency, which is consistent with the previous research [19,38]. The reason might be because the OH^- in the solution not only generated electrostatic interaction with the La^{3+} and Fe^{3+} on the surface of the adsorbent but also competed with the adsorption sites, resulting in the decrease of the adsorption sites. As shown in Fig. 9b, the pH increased at low pH after the adsorption, which might be due to that fluoride ions replaced the OH^- on the surface of the adsorbent.

3.10. Effects of adsorbent dosage on the fluoride removal

Fig. 10 shows the influence of the amount of adsorbent on the removal efficiency and adsorption capacity of fluoride. The initial concentration of fluoride was set to 10 mg/L, the shaking time was set to 5 h, and the pH value was pristine. The amount of adsorbent added was 0.01, 0.03, 0.05, 0.07, 0.09, 0.11, 0.13, 0.15 g/50 mL, respectively. As can be seen, the adsorption efficiency increased from 47.90% to 98.58%, while the adsorption capacity gradually decreased from 23.95 to 3.29 mg/g with the increase of the adsorbent dosage. This result is similar to the work of Chen et al. [49].

3.11. Effects of the initial concentration of fluoride on the fluoride removal

Fig. 11 shows the effect of the initial concentration of fluoride on the fluoride removal over Fe-La-WBC-300 at

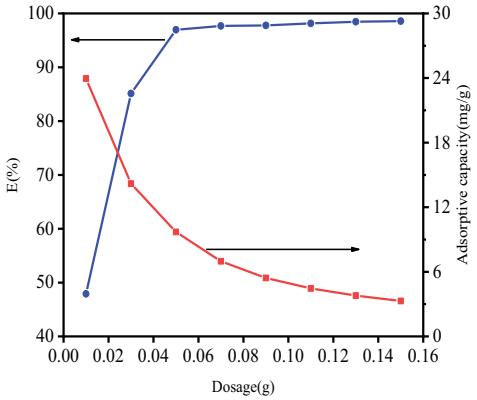

Fig. 10. Effects of adsorbent dosage on fluoride removal over Fe-La-WBC-300 at 298 K.

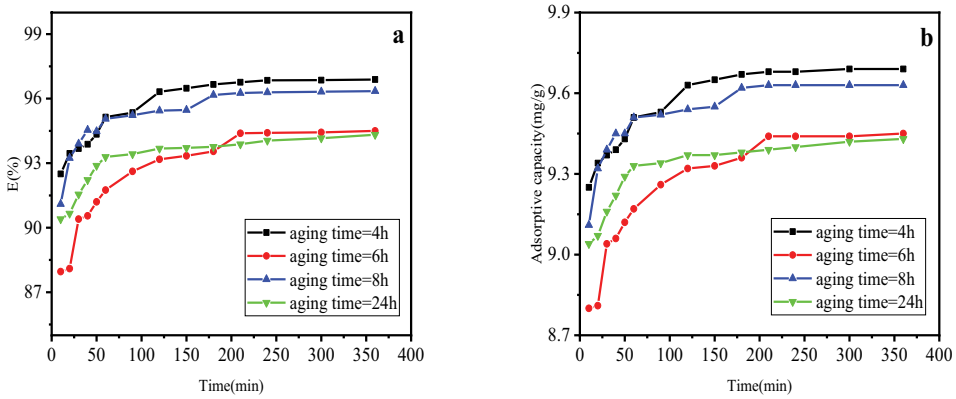

Fig. 8. Fluoride removal with the oscillation time and the aging time on Fe-La-WBC-300 at 298 K. (a) *E*(%) and (b) adsorption capacity.

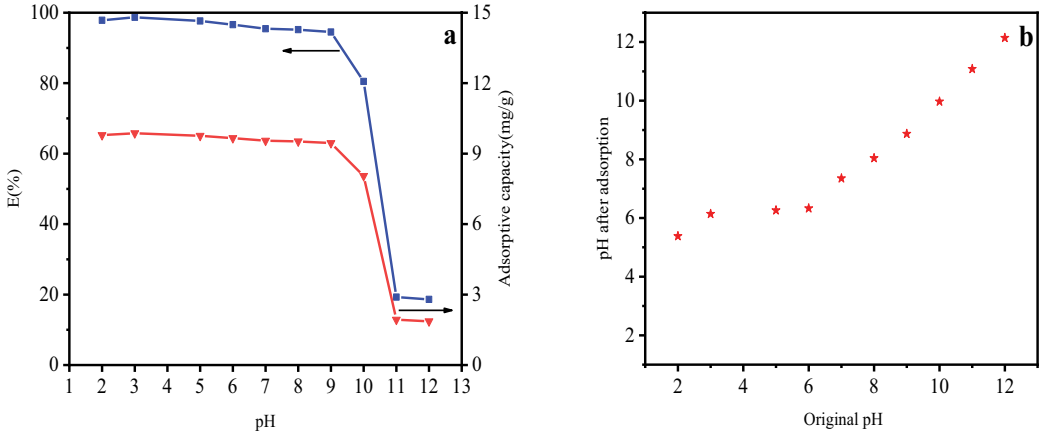

Fig. 9. (a) Variation of *E*(%) and adsorption capacity (mg/g) of fluoride with pH at 298 K and (b) pH of the solution after adsorption.

298 K. The amount of adsorbent added was 0.05 g/50 mL, the pH value was not adjusted, the shaking time was 5 h, and the initial concentration of fluoride was 5, 10, 20, 40, 50, 80, and 100 mg/L, respectively. As can be seen, with the increase of the initial concentration of fluoride, the adsorption efficiency decreases, whereas the adsorption capacity keeps increasing. The decrease of the adsorption efficiency is due to the decrease of the available sites on the adsorbent with the increase of the initial concentration [50]. It can be found that the same dosage of adsorbent has similar fluoride removal efficiency for the initial concentrations of 5 and 10 mg/L, which is because the available sites of the adsorbent are sufficient for the fluoride. For a fluoride concentration of 10 mg/L, the maximum adsorption efficiency was 96.95%.

3.12. Effects of contact time on the fluoride removal and the adsorption kinetics

The influence of the oscillation time on the fluoride adsorption over Fe-La-WBC-300 at 298 K is shown in Fig. 12. The initial concentration of fluoride was 5, 10, 20, and 50 mg/L, the pH value was pristine, and the amount of adsorbent added was 0.05 g/50 mL. For the initial fluoride concentrations of 5 and 10 mg/L, the efficiency reached more than 90% in the first 30 min. Then, the removal efficiency slowly increased with time and the adsorption reached equilibrium after 5 h. Further increase of the fluoride concentration to 20 and 50 mg/L decreased the removal efficiency, which might be because all the adsorbent sites were empty at the beginning and the solute concentration gradient was high. The adsorption capacity shows a similar changing trend with the adsorption efficiency.

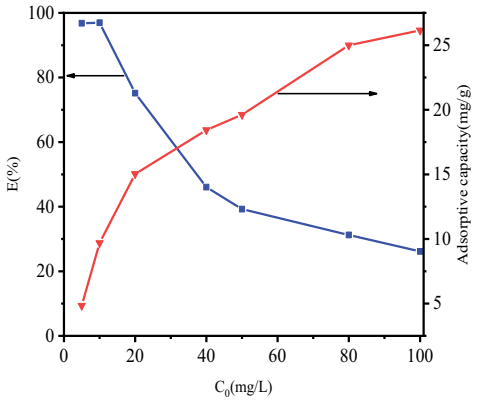

Fig. 11. Effects of initial fluoride concentration on the removal over Fe-La-WBC-300 at 298 K.

Kinetic studies can help to understand the adsorption mechanism by analyzing the relationship between the adsorbate concentration and the time. The adsorption data were often fitted into two classical kinetic models, namely, the pseudo-first-order and pseudo-second-order models. Meanwhile, we also studied the intraparticle diffusion model to determine whether the reaction rate was the determining step of the adsorption process.

Pseudo-first-order kinetics uses Eq. (3) [51]:

$$\ln\left(Q_e - Q_t\right) = \ln Q_e - k_1 t \tag{3}$$

Pseudo-second-order kinetics uses Eq. (4) [52]:

$$\frac{t}{Q_t} = \frac{1}{k_2 Q_e^2} + \frac{t}{Q_e} \tag{4}$$

Intraparticle diffusion model uses Eq. (5) [53]:

$$Q_t = k_p t^{1/2} + E \tag{5}$$

where Q_e and Q_t are the adsorption capacity at equilibrium and at any time t, mg/g; k_1 and k_2 are rate constant of the pseudo-first-order kinetics, min^{-1} and the pseudo-second-order kinetics, g/mg·min, respectively; k_p is rate diffusion constants within the particles, mg/(kg·$min^{1/2}$); E is a constant related to the boundary layer thickness, mg/g.

The kinetics parameters of the fluoride adsorption with initial concentrations of 5, 10, 20, and 50 mg/L were explored and are shown in Table 3. The average linear regression coefficient between $\ln(Q_e - Q_t)$ and t of pseudo-first-order kinetics is only 0.874, as shown in Fig. 13a. Also, Q_e(calculated) and Q_e(exp) show high discrepancy, indicating that the pseudo-first-order kinetic is not suitable for the fluoride adsorption of Fe-La-WBC-300. By drawing the linear relationship between t/Q_t and t, the average

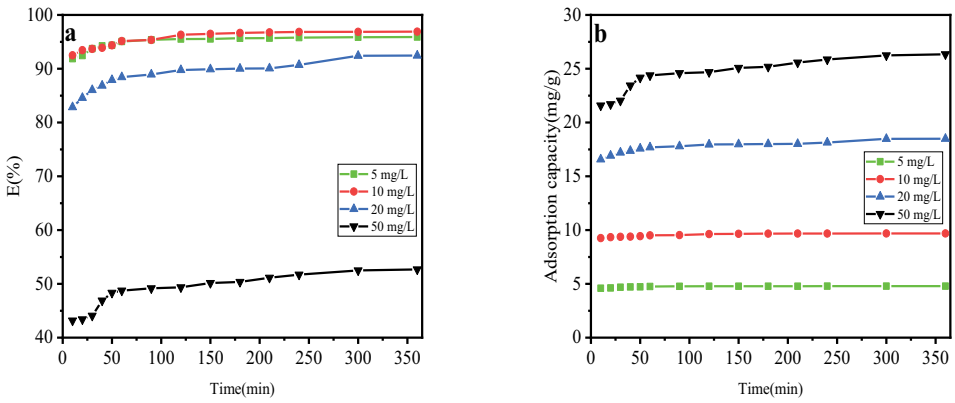

Fig. 12. Effects of time on fluoride removal over Fe-La-WBC-300 at 298 K. (a) E(%) and (b) adsorptive capacity.

Table 3
Kinetic parameters of the fluoride adsorption over Fe-La-WBC-300 at 298 K

Kinetics	Parameters	Fluoride concentration (mg/L)			
		5	10	20	50
Pseudo-first-order	k_1 (min^{-1})	0.0150	0.0176	0.0123	0.0109
	R^2	0.954	0.984	0.658	0.900
	Q_e(calculated) (mg/g)	0.159	0.554	2.252	5.238
	Q_e(exp) (mg/g)	4.79	9.69	18.49	26.34
Pseudo-second-order	k_2 [g/(mg·min)]	0.2943	0.0878	0.0219	0.0071
	R^2	1	0.9999	0.9997	0.9994
	Q_e(calculated) (mg/g)	4.80	9.73	18.40	26.35
	Q_e(exp) (mg/g)	4.79	9.69	18.49	26.34

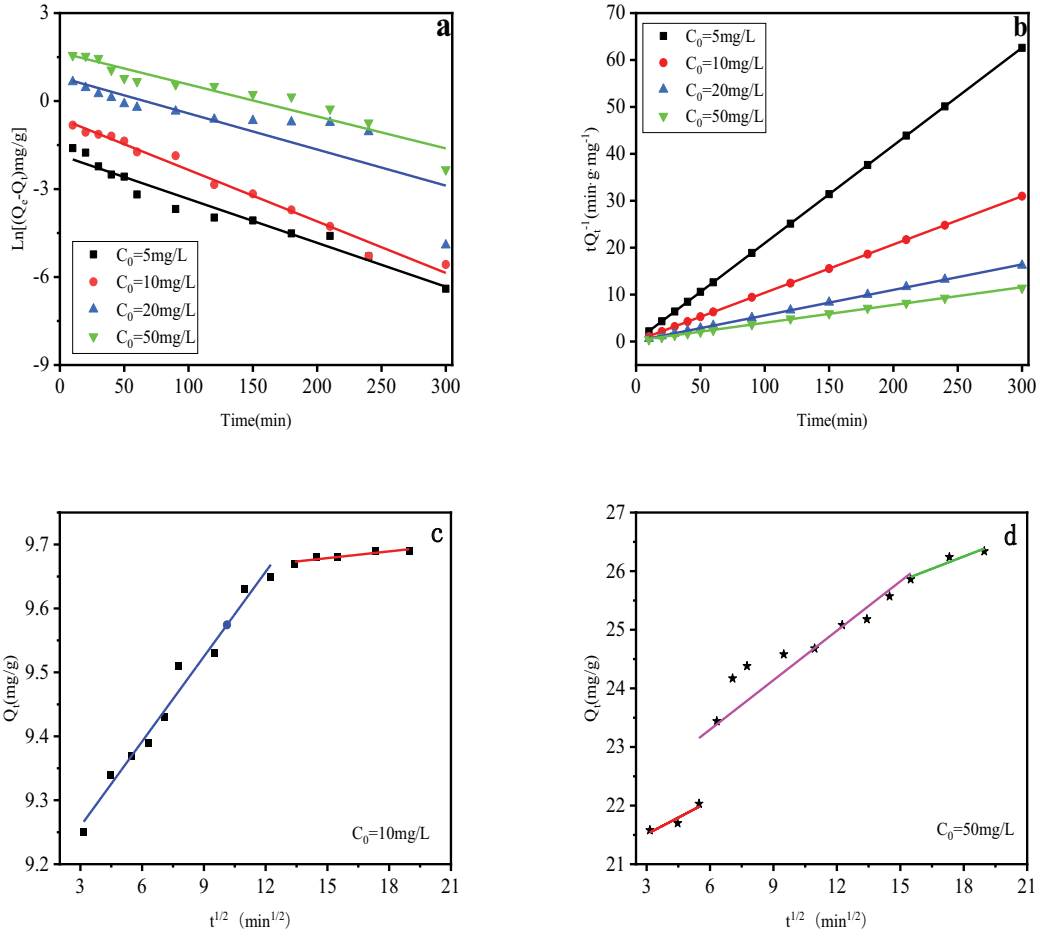

Fig. 13. Adsorption kinetic fitting of (a) pseudo-first-order model, (b) pseudo-second-order model, (c) intraparticle diffusion fitting curve (C_0 = 10 mg/L) and (d) intraparticle diffusion fitting curve (C_0 = 50 mg/L).

linear regression coefficient reaches up to 0.9998, as shown in Fig. 13b. In addition, the value of Q_e(calculated) is very close to Q_e(exp), indicating that the adsorption process of fluoride follows pseudo-second-order kinetics. The pseudo-second-order model means that chemical adsorption is the main control factor for the adsorption [54]. The calculated value of k_2 varies from 0.2943 to 0.0071 g/mg·min with the decrease of the fluoride concentration.

By fitting the linear relationship of Q_t and $t^{1/2}$, the fitting coefficient was obtained in Fig. 13c and d. The intraparticle diffusion parameters of the fluoride adsorption with initial concentrations of 10 and 50 mg/L were explored and are shown in Table 4. As shown in Fig. 13c, when the initial concentration of fluorine ion was 10 mg/L, the first 150 min was in the rapid adsorption phase with a k_p of 0.2376; when the adsorption time was 150–360 min, the adsorption achieved

Table 4
Intraparticle diffusion of the fluoride adsorption over Fe-La-WBC-300 at 298 K

Fluoride concentration (mg/L)	Parameters	Surface adsorption	Internal diffusion	Adsorption equilibrium
	k_p [mg/(kg·min$^{1/2}$)]	0.2367	0.2367	0.0282
10	R^2	0.976	0.976	0.881
	E (mg/g)	8.82	8.82	9.57
	k_p [mg/(kg·min$^{1/2}$)]	0.189	0.281	0.139
50	R^2	0.890	0.813	0.915
	E (mg/g)	20.94	21.61	23.74

balance with a k_p of 0.0282. As shown in Fig. 13d, when the initial concentration of fluoride ion was 50 mg/L, the first 240 min was in the rapid adsorption stage; when the adsorption time was 300–360 min, the adsorption basically reached the equilibrium state with a k_p of 0.139 [55]. In sum, the correlation coefficient obtained by the intraparticle diffusion model for fitting the experimental data is not very high, which cannot show whether the intraparticle diffusion is a rate-determining step or not.

3.13. Adsorption isotherms

By using adsorption isotherm based on the relationship between the adsorbate concentration and the adsorption capacity at equilibrium, the theoretical maximum adsorption capacity per absorbent can be obtained and the adsorption mechanism can be explored. The Langmuir isotherm is based on the theory of monolayer adsorption using Eq. (6), while the Freundlich isotherm is often used for multiphase or multilayer adsorption under non-ideal conditions as Eq. (7) [56].

$$\frac{C_e}{Q_e} = \frac{C_e}{Q_{\max}} + \frac{1}{K_L Q_{\max}} \tag{6}$$

$$\log Q_e = \frac{\log C_e}{n} + \log K_F \tag{7}$$

where C_e is the fluoride concentration at equilibrium, mg/L; Q_e is the equilibrium adsorption capacity, mg/g; $Q_{\max}$ is the saturated adsorption capacity, mg/g; K_L is the Langmuir constant, L/mg; K_F is the Freundlich constant, L/mg; n is the concentration constant.

Fig. 14 shows the Freundlich and Langmuir isotherm curves of the fluoride adsorption process of Fe-La-WBC-300. In the experiments, 0.05 g adsorbent was added to 50 mL solutions with fluoride concentrations of 5, 10, 20, 40, 50, 80, and 100 mg/L and stirred for 5 h. The calculated K_L, K_F, and $Q_{\max}$ by Eqs. (6) and (7) and R^2 are listed in Table 5. As can be seen, the Freundlich model has a higher R^2 than the Langmuir model at 298 and 318 K, while the latter has a slightly higher R^2 than the former at 308 and 328 K. The R^2 value of the Langmuir model is greater than that of the Freundlich model when the pH is 3, 7, and 9. This indicates that there are multiple layers of active sites for fluoride adsorption on the surface of Fe-La-WBC-300 and the adsorption may be molecular layer adsorption and there are interactions between adjacent adsorbed molecules [57]. Meanwhile, there may also be the adsorption of the molecular layer.

The separation coefficient, R_L, can be used to judge whether it is conducive to the adsorption, which can be calculated using Eq. (8):

$$R_L = \frac{1}{1 + K_L \times C_0} \tag{8}$$

Table 6 lists the R_L values of different C_0 of fluoride. All the R_L values are in the range 0–1, indicating the process of adsorbing fluoride is favorable [3]. In addition, the value of the Freundlich constant (n) is in the range of 0–1, indicating that Fe-La-WBC-300 has better performance in fluoride removal.

Table 7 lists the comparison of the reported adsorption capacity and our work. The adsorption capacity of Fe-La-WBC-300 in our work at 298 K is 21.78 mg/g, which is greater than those in the literature.

3.14. Effects of temperature on fluoride removal and the adsorption thermodynamics

Fig. 15 shows the effects of temperatures on the fluoride adsorption over Fe-La-WBC-300. In the experiment, the initial concentration of the fluoride solution was 5, 10, 20, 40, 50, 80, 100 mg/L, the amount of adsorbent was 0.05 g/50 mL, the temperature of the water bath was 298, 308, 318, and 328 K, and the oscillation time was 5 h. It can be found that the adsorption capacity increases with the increase of the temperature, which might be caused by the random thermal movement of fluoride ions, and the probability of collision between fluoride ions and adsorption sites increase as the temperature increases [63].

The thermodynamic parameters, ΔS, ΔH, and ΔG, in the adsorption process, can be obtained by using Van't Hoff and Gibbs–Helmholtz Eqs. (9) and (10). The equilibrium constant of the adsorption, K_e, can be obtained using Eq. (11) [64].

$$\ln K_e = \frac{\Delta S^\circ}{R} - \frac{\Delta H^\circ}{RT} \tag{9}$$

$$\Delta G^\circ = \Delta H^\circ - T\Delta S^\circ \tag{10}$$

$$K_e = \alpha \frac{Q_e}{C_e} \tag{11}$$

where ΔG°, ΔH° and ΔS°, represent the standard Gibbs energy change, standard enthalpy change, and standard

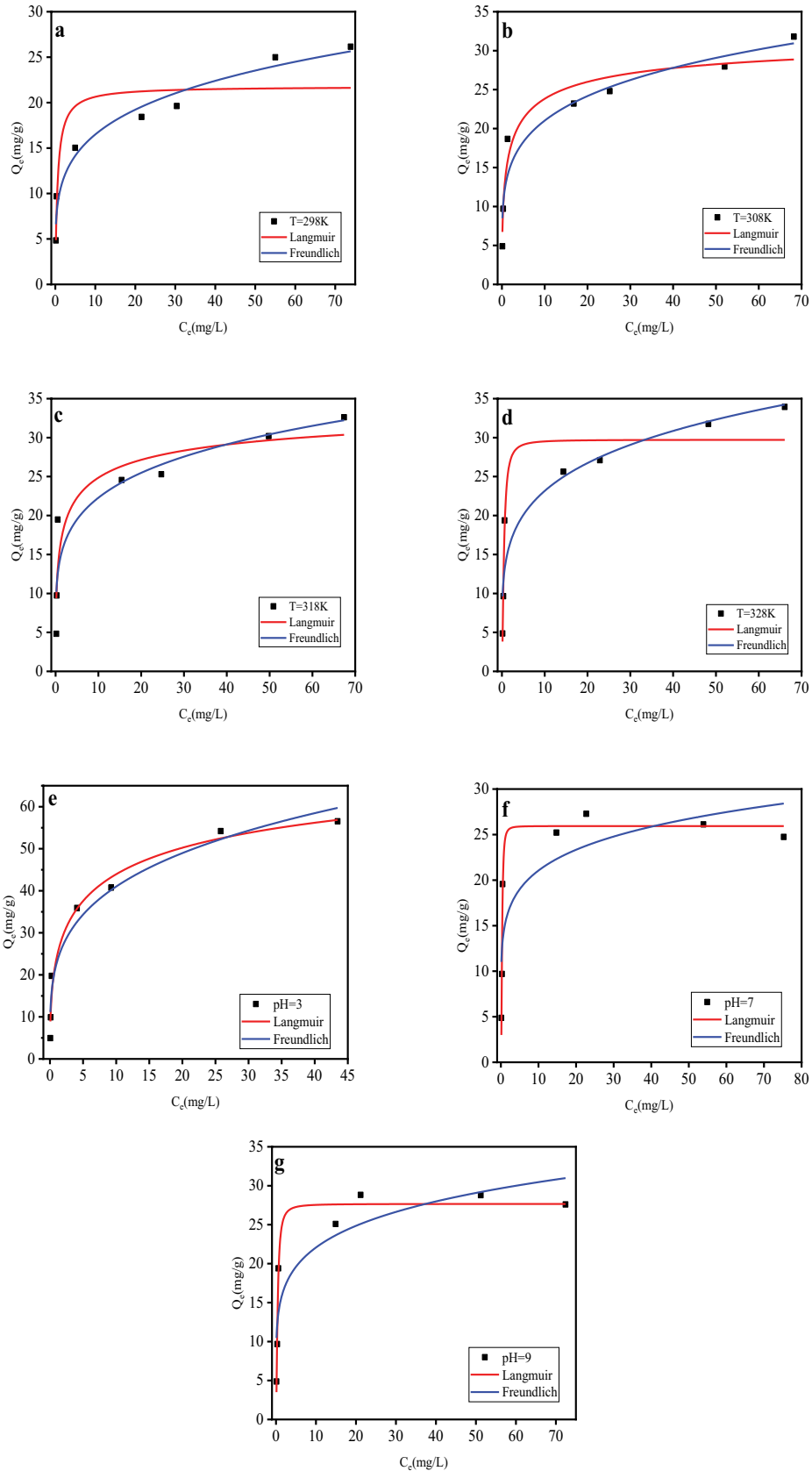

Fig. 14. Isotherm adsorption on Fe-La-WBC-300 fitted by the Langmuir and Freundlich model. (a) T = 298 K, (b) T = 308 K, (c) T = 318 K, (d) T = 328 K, (e) pH = 3, (f) pH = 7 and (g) pH = 9.

Table 5
Fitted parameters of the Langmuir and Freundlich isotherm model

	Langmuir			Freundlich		
	Q_{max} (mg/g)	K_L (L/mg)	R^2	K_F (L/mg)	1/n	R^2
T = 298 K	21.78	1.800	0.775	9.928	0.2206	0.958
T = 308 K	33.04	0.793	0.925	13.226	0.2013	0.921
T = 318 K	36.17	0.772	0.820	14.28	0.1934	0.849
T = 328 K	29.72	3.392	0.898	14.38	0.2070	0.889
pH = 3	84.61	0.396	0.971	22.75	0.2560	0.959
pH = 7	25.93	13.32	0.948	14.96	0.1485	0.696
pH = 9	27.67	4.614	0.961	14.88	0.1713	0.792

Table 6
R_L of different C_0 of fluoride

K_L / C_0	T = 298 K	T = 308 K	T = 318 K	T = 328 K	pH = 3	pH = 7	pH = 9
	1.800	0.793	0.772	3.392	0.396	13.32	4.614
5 mg/L	0.1000	0.2014	0.2058	0.0557	0.3356	0.0148	0.0415
10 mg/L	0.0526	0.1120	0.1147	0.0286	0.2016	0.0075	0.0212
20 mg/L	0.0270	0.0593	0.0608	0.0145	0.1121	0.0037	0.0107
40 mg/L	0.0137	0.0306	0.0314	0.0073	0.0594	0.0019	0.0054
50 mg/L	0.0110	0.0246	0.0253	0.0059	0.0481	0.0015	0.0043
80 mg/L	0.0069	0.0155	0.0159	0.0037	0.0306	0.0009	0.0027
100 mg/L	0.0055	0.0125	0.0128	0.0029	0.0246	0.0008	0.0022

Table 7
Comparison of the adsorption between the reported fluoride adsorbents with this work

Adsorbent	Initial concentration of F^- (mg/L)	Dosage (g/L)	Adsorption capacity (mg/g)	References
La(III)-modified alumina	10	1.25	7.0	[51]
La(III)-modified GAC	20	0.1	9.96	[37]
Fe@ABDC	10	2	4.92	[58]
NaOH/Fe-MFA	10	2	19.8	[59]
WMRBC	50	0.05	9.5	[32]
WH-HAO	5	1	4.43	[60]
Commercial bituminous activated carbon impregnated with La	20	3.3	5.93	[61]
Chitosan-zeolite composite modified with La(III)	20	2	14.3	[62]
Fe-La-WBC-300	10	1.0	21.78	This work

entropy change of the adsorption process, T is the absolute temperature (K), R is the universal gas constant (8.314J/K·mol), K_e is the equilibrium constant, and α is the adsorbent amount (g/L).

Fig. 16 shows the linear plot of lnK_e to 1/T at 298, 308, and 318 K. The initial concentration of the fluorine solution was 10 mg/L, the adsorbent dosage was 0.05 g/50 mL, and the adsorption time was 5 h. The calculated thermodynamic parameters are tabulated in Table 8. The positive $\Delta H°$ (27.36 kJ/mol) of the fluoride adsorption shows that the adsorption is chemical adsorption and high temperature is favorable for the reaction, which is also consistent with the literature. The positive $\Delta S°$ corresponds to the increase in entropy during the adsorption process over Fe-La-WBC-300. The negative $\Delta G°$ means the spontaneous nature and feasibility of the fluoride adsorption process at the above temperature [65].

3.15. Effects of coexisting ions on the fluoride removal

The coexisting anions compete with fluoride for adsorption sites, which might decrease the removal efficiency. Fig. 17 shows the influence of the concentration of competing anions on fluoride removal. In these experiments, the initial

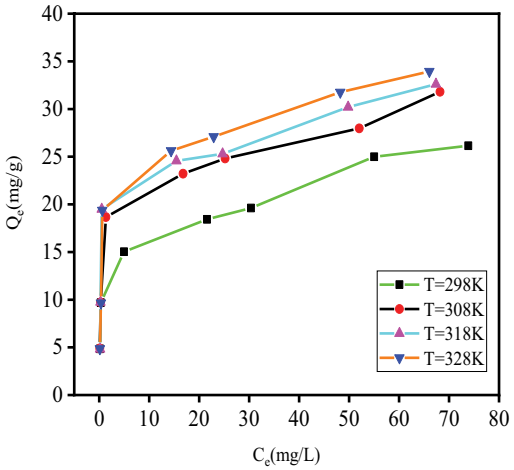

Fig. 15. Effects of temperature on fluoride removal over Fe-La-WBC-300.

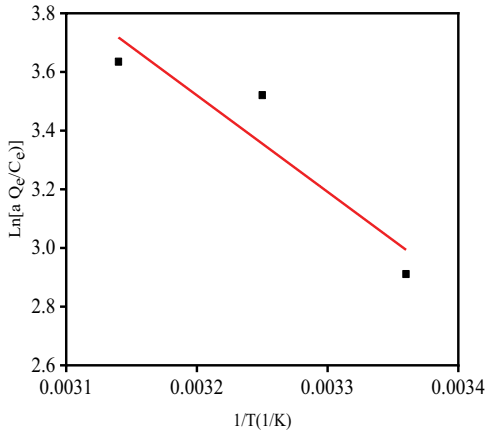

Fig. 16. Plot of lnK_e to 1/T of Fe-La-WBC-300.

Table 8
Thermodynamic parameters of fluoride adsorption over Fe-La-WBC-300

Temperature (K)	$\Delta H°$ (kJ/mol)	$\Delta S°$ (J/K·mol)	$\Delta G°$ (kJ/mol)
298	27.36	116.8	−7.446
308	27.36	116.8	−8.614
318	27.36	116.8	−9.782

fluorine concentration was 10 mg/L, the adsorption time was 5 h, the adsorbent amount was 0.05 g/50 mL, the initial pH value was pristine, and the concentration of interfering ions was 50, 100, 200, 500, and 1,000 mg/L. As seen in the figure, Cl^- has almost no effects on the fluoride removal efficiency, and SO_4^{2-} reduces the removal efficiency as its concentration increases. However, even if the concentration of PO_4^{3-} is only 50 mg/L, the fluorine removal efficiency significantly decreases. CO_3^{2-} has a greater inhibitory effect on fluoride removal than any other anions [66]. By comparison, the order for the inhibitory of fluoride removal by the five anions is $CO_3^{2-} > HCO_3^- > PO_4^{3-} > SO_4^{2-} > Cl^-$.

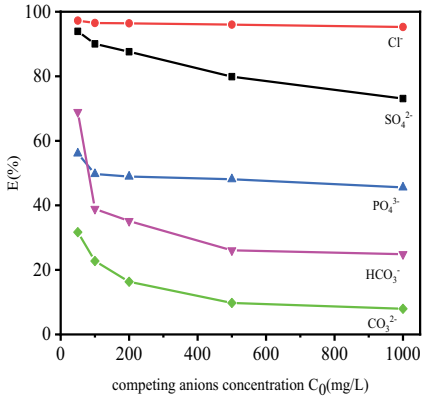

Fig. 17. Effects of competing ions on fluoride removal (Cl^-, SO_4^{2-}, PO_4^{3-}, CO_3^{2-}, HCO_3^-).

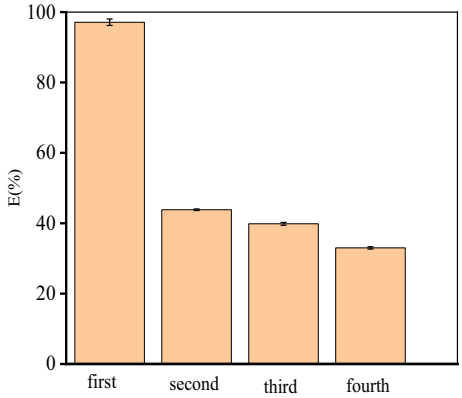

Fig. 18. Recycling performance of Fe-La-WBC-300 for fluoride removal.

3.16. Reusability of the adsorbent

Fig. 18 shows the recycling test of the Fe-La-WBC-300 for fluoride removal. The initial fluoride concentration was 10 mg/L, the amount of adsorbent was 0.05 g/50 mL, the shaking time was 5 h, the temperature was 298 K, and the pH of the solution maintained its original value. Before the next adsorption, the adsorbent was filtered and dried in an incubator, then soaked in 5% sodium hydroxide solution for 12 h, washed with distilled water to neutral, and finally dried in an oven [67]. The adsorption efficiency of the first cycle was 97.32%, which decreased to 43.58%, 40.11%, and 33.32% in the following cycles. The results show that the re-usability of the adsorbent needs to be further studied to find a more suitable elution method.

3.17. Application to groundwater sample

To test the adsorption effect of fluoride in actual groundwater samples, Nanpocun village around our campus was selected as the actual groundwater sample collection point. The groundwater was collected under 30 m with a clear and transparent appearance. The physical and chemical properties of the groundwater are shown in Table 9, in which the pH was 8.57, and the fluoride concentration was 0.19 mg/L.

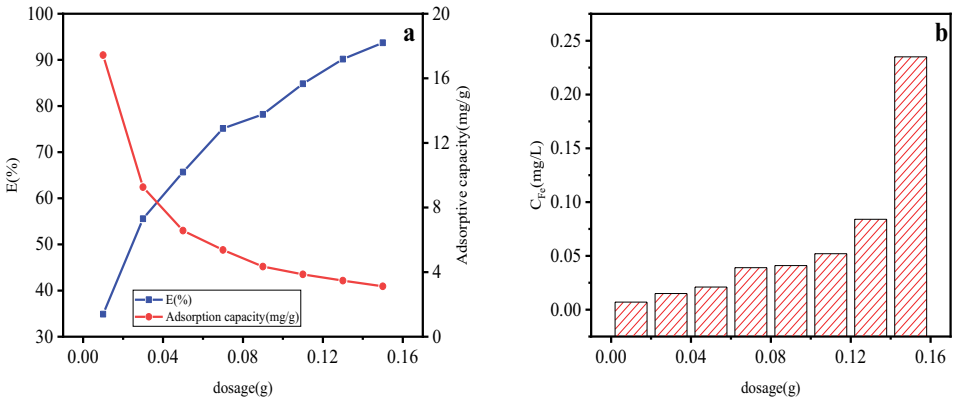

Fig. 19. (a) Effects of dosage of Fe-La-WBC-300 on fluoride removal in real water and (b) the leaching iron ions concentration with different dosage.

Table 9
Main components of groundwater collected from Nanpocun village

Items	Value	Items	Value
pH	8.57	CO_3^{2-} (mg/L)	40
F^- (mg/L)	0.19	HCO_3^- (mg/L)	336
Cl^- (mg/L)	23.3	NH_3–N (mg/L)	ND
NO_3^- (mg/L)	0.3	K^+ (mg/L)	0.85
TDS (mg/L)	480	Ca^{2+} (mg/L)	3.69
NO_2^- (mg/L)	0.008	Na^+ (mg/L)	184
ND means under the detection limit.			
TDS means total dissolved solids.			

Since the actual fluorine concentration in groundwater was only 0.19 mg/L, which did not exceed the standard, the fluorine concentration was increased to 10 mg/L by adding fluorine to the water sample [32]. The adsorption performance of Fe-La-WBC-300 in the actual water was studied and the results were shown in Fig. 19a. In the experiment, the adsorption time was 5 h, and the temperature was 298 K. As shown in Fig. 19a, as the adsorbent dosage increases from 0.01 to 0.15 g/50 mL, the removal efficiency increases, whereas the adsorption capacity gradually decreases. The highest removal efficiency was 93.70%, corresponding to an adsorption capacity of 3.12 mg/g. Fig. 19b shows the measured leaching iron concentration varied with the amounts of adsorbent. As the dosage of adsorbent increases, the amount of iron concentration gradually increases. When the dosage was 0.13 g/50 mL, the leaching iron ion concentration was 0.084 mg/L. Both the fluoride and iron ion concentration were lower than the limits of fluoride concentration (1.0 mg/L) and iron concentration (0.3 mg/L) required in GB/T 14848-2017.

4. Conclusions

- Iron and lanthanum were loaded on the watermelon rind biochar by a co-precipitation method. The best conditions for the static adsorption process of 10 mg/L fluoride were: pH was in the range 2–9, the amount of adsorbent was 0.05 g/50 mL, and the reaction time was 5 h. The high removal efficiency in a wide pH range was suitable for extensive applicability.
- The correlation coefficient (R^2) of the Freundlich model was better than that of the Langmuir model. The adsorption process follows a pseudo-second-order kinetic model. Metal complexation, ion exchange, and electrostatic attraction were the main adsorption mechanisms for the fluoride removal. The adsorption process is spontaneous with a negative Gibbs free energy.
- In the actual groundwater adsorption experiment, the fluorine removal efficiency reached 93.70% and the adsorption capacity reached 17.44 mg/g, which had application prospects for its highly effective and low-cost solution to the problem of fluoride pollution in aqueous environments.

Acknowledgments

The authors thank the support from the National Natural Science Foundation of China under grant No. 51978556 and Major Scientific and Technological Innovation Projects of Shandong Province under grant No. 2019JZZY010343.

Data availability statement

The authors confirm that the data supporting the findings of this study are all available within the article [and/or] its supplementary materials.

References

[1] A. Vinati, B. Mahanty, S.K. Behera, Clay and clay minerals for fluoride removal from water: a state-of-the-art review, Appl. Clay Sci., 114 (2015) 340–348.
[2] A.K. Tiwari, A.K. Singh, M.K. Mahato, GIS based evaluation of fluoride contamination and assessment of fluoride exposure dose in groundwater of a district in Uttar Pradesh, India, Hum. Ecol. Risk Assess., 23 (2017) 56–66.
[3] P. Liang, R. An, R. Li, D. Wang, Comparison of La^{3+} and mixed rare earths-loaded magnetic chitosan beads for fluoride adsorption, Int. J. Biol. Macromol., 11 (2018) 255–263.
[4] A. Ghosh, K. Mukherjee, S.K. Ghosh, B. Saha, Sources and toxicity of fluoride in the environment, Res. Chem. Intermed., 39 (2013) 2881–2915.

[5] Z. Bonyadi, P.S. Kumar, R. Foroutan, R. Kafaei, H. Arfaeinia, S. Farjadfard, B. Ramavandi, Ultrasonic-assisted synthesis of *Populus alba* activated carbon for water defluorination: application for real wastewater, Korean J. Chem. Eng., 36 (2019) 1595–1603.
[6] R. Foroutan, R. Zareipour, R. Mohammadi, Fast adsorption of chromium(VI) ions from synthetic sewage using bentonite and bentonite/bio-coal composite: a comparative study, Mater. Res. Express, 6 (2018) 025508, doi: 10.1088/2053-1591/aaebb9.
[7] B. Naeimi, R. Foroutan, B. Ahmadi, F. Sadeghzadeh, B. Ramavandi, Pb(II) and Cd(II) removal from aqueous solution, shipyard wastewater, and landfill leachate by modified *Rhizopus oryzae* biomass, Mater. Res. Express, 5 (2018) 045501, doi: 10.1088/2053-1591/aab81b.
[8] A. Savari, S. Hashemi, H. Arfaeinia, S. Dobaradaran, R. Foroutan, A.H. Mahvi, B. Ramavandi, Physicochemical characteristics and mechanism of fluoride removal using powdered zeolite-zirconium in modes of pulsed& continuous sonication and stirring, Adv. Powder Technol., 31 (2020) 3521–3532.
[9] S. Abbasi, R. Foroutan, H. Esmaeili, F. Esmaeilzadeh, Preparation of activated carbon from worn tires for removal of Cu(II), Ni(II) and Co(II) ions from synthetic wastewater, Desal. Water Treat., 141 (2019) 269–278.
[10] V. Kimambo, P. Bhattacharya, F. Mtalo, J. Mtamba, A. Ahmad, Fluoride occurrence in groundwater systems at global scale and status of defluoridation – state of the art, Groundwater Sustainable Dev., 9 (2019) 100223, doi: 10.1016/j.gsd.2019.100223.
[11] J. Borah, D. Saikia, Estimation of the concentration of fluoride in the groundwater of Tinsukia town master plan area of the Tinsukia district, Assam, India, Arch. Appl. Sci. Res., 3 (2011) 202–206.
[12] S. Mukherjee, P. Sahu, G. Halder, Microbial remediation of fluoride-contaminated water via a novel bacterium *Providencia vermicola* (KX926492), J. Environ. Manage., 204 (2017) 413–423.
[13] K. Biswas, K. Gupta, A. Goswami, U.C. Ghosh, Fluoride removal efficiency from aqueous solution by synthetic iron(III)–aluminum(III)–chromium(III) ternary mixed oxide, Desalination, 255 (2010) 44–51.
[14] S. Budyanto, Y.L. Kuo, J.C. Liu, Adsorption and precipitation of fluoride on calcite nanoparticles: a spectroscopic study, Sep. Purif. Technol., 150 (2015) 325–331.
[15] M. Grzegorzek, K. Majewska-Nowak, A.E. Ahmed, Removal of fluoride from multicomponent water solutions with the use of monovalent selective ion-exchange membranes, Sci. Total Environ., 722 (2020) 137681, doi: 10.1016/j.scitotenv.2020.137681.
[16] I. Owusu-Agyeman, M. Reinwald, A. Jeihanipour, A.I. Schäfer, Removal of fluoride and natural organic matter from natural tropical brackish waters by nanofiltration/reverse osmosis with varying water chemistry, Chemosphere, 217 (2019) 47–58.
[17] J. Shen, A. Schäfer, Removal of fluoride and uranium by nanofiltration and reverse osmosis: a review, Chemosphere, 117 (2014) 679–691.
[18] V. Khatibikamal, A. Torabian, F. Janpoor, G. Hoshyaripour, Fluoride removal from industrial wastewater using electrocoagulation and its adsorption kinetics, J. Hazard. Mater., 179 (2010) 276–280.
[19] J. Wang, L. Wu, J. Li, D. Tang, G. Zhang, Simultaneous and efficient removal of fluoride and phosphate by Fe-La composite: adsorption kinetics and mechanism, J. Alloys Compd., 753 (2018) 422–432.
[20] R.M. Hegde, R.M. Rego, K.M. Potla, M.D. Kurkuri, M. Kigga, Bio-inspired materials for defluoridation of water: a review, Chemosphere, 253 (2020) 126657, doi: 10.1016/j.chemosphere.2020.126657.
[21] S. Wan, J. Lin, W. Tao, Y. Yang, Y. Li, F. He, Enhanced fluoride removal from water by nanoporous biochar-supported magnesium oxide, Ind. Eng. Chem. Res., 58 (2019) 9988–9996.
[22] L. Mei, H. Qiao, F. Ke, C. Peng, R. Hou, X. Wan, H. Cai, One-step synthesis of zirconium dioxide-biochar derived from *Camellia oleifera* seed shell with enhanced removal capacity for fluoride from water, Appl. Surf. Sci., 509 (2020) 144685, doi: 10.1016/j.apsusc.2019.144685.
[23] V. Meilani, J.-I. Lee, J.-K. Kang, C.-G. Lee, S. Jeong, S.J. Park, Application of aluminum-modified food waste biochar as adsorbent of fluoride in aqueous solutions and optimization of production using response surface methodology, Microporous Mesoporous Mater., 312 (2021) 110764, doi: 10.1016/j.micromeso.2020.110764.
[24] I. Anastopoulos, A. Bhatnagar, E.C. Lima, Adsorption of rare earth metals: a review of recent literature, J. Mol. Liq., 221 (2016) 954–962.
[25] T. Getachew, A. Hussen, V.M. Rao, Defluoridation of water by activated carbon prepared from banana (*Musa paradisiaca*) peel and coffee (*Coffea arabica*) husk, Int. J. Environ. Sci. Technol., 12 (2015) 1857–1866.
[26] R.L. Zhang, J. Xu, L. Gao, Z. Wang, B. Wang, S.Y. Qin, Performance and mechanism for fluoride removal in groundwater with calcium modified biochar from peanut shell, Sci. Technol. Adv. Mater., 12 (2020) 492–501.
[27] B.D. Gebrewold, P. Kijjanapanich, E.R. Rene, P.N. Lens, Fluoride removal from groundwater using chemically modified rice husk and corn cob activated carbon, Environ. Technol., 40 (2019) 2913–2927.
[28] Q.F. Tian, J. Sun, Study on the adsorption of fluorine by tea, Chem. Bioeng., 28 (2011) 29–31.
[29] M. Keiluweit, P.S. Nico, M.G. Johnson, M. Kleber, Dynamic molecular structure of plant biomass-derived black carbon (biochar), Environ. Sci. Technol., 44 (2010) 1247–1253.
[30] Z.Q. Li, C.J. Lu, Z.P. Xia, Y. Zhou, Z. Luo, X-ray diffraction patterns of graphite and turbostratic carbon, Carbon, 45 (2007) 1686–1695.
[31] W. Wu, M. Yang, Q. Feng, K. McGrouther, H. Wang, H. Lu, Y. Chen, Chemical characterization of rice straw-derived biochar for soil amendment, Biomass Bioenergy, 47 (2012) 268–276.
[32] M. Sadhu, P. Bhattacharya, M. Vithanage, P.P. Sudhakar, Adsorptive removal of fluoride using biochar – a potential application in drinking water treatment, Sep. Purif. Technol., 278 (2021) 119106, doi: 10.1016/j.seppur.2021.119106.
[33] J. Wang, N. Chen, C. Feng, M. Li, Performance and mechanism of fluoride adsorption from groundwater by lanthanum-modified pomelo peel biochar, Environ. Sci. Pollut. Res., 25 (2018) 15326–15335.
[34] N.B. Dewage, A.S. Liyanage, C.U. Pittman Jr., D. Mohan, T. Mlsna, Fast nitrate and fluoride adsorption and magnetic separation from water on α-Fe_2O_3 and Fe_3O_4 dispersed on Douglas fir biochar, Bioresour. Technol., 263 (2018) 258–265.
[35] D. Thakre, S. Jagtap, A. Bansiwal, N. Labhsetwar, S. Rayalu, Synthesis of La-incorporated chitosan beads for fluoride removal from water, J. Fluorine Chem., 131 (2010) 373–377.
[36] G. Li, C. Li, Z. Xu, Z. Cheng, J. Lin, Facile synthesis, growth mechanism and luminescence properties of uniform $La(OH)_3$:Ho^{3+}/Yb^{3+} and La_2O_3:Ho^{3+}/Yb^{3+} nanorods, CrystEngComm, 12 (2010) 4208–4216.
[37] E. Vences-Alvarez, L.H. Velazquez-Jimenez, L.F. Chazaro-Ruiz, P.E. Diaz-Flores, J.R. Rangel-Mendez, Fluoride removal in water by a hybrid adsorbent lanthanum-carbon, J. Colloid Interface Sci., 455 (2015) 194–202.
[38] D.K. Liu, H. Liu, L. Yang, Y.M. Luo, C.Y. Han, Adsorption of fluoride ion by lanthanum and cerium modified mesoporous alumina, Mater. Rev., 33 (2019) 590–594.
[39] S.H. Dhawane, A.A. Khan, K. Singh, A. Tripathi, R. Hasda, G. Halder, Insight into optimization, isotherm, kinetics, and thermodynamics of fluoride adsorption onto activated alumina, Environ. Prog. Sustainable Energy, 37 (2018) 766–776.
[40] D. Tang, G. Zhang, Efficient removal of fluoride by hierarchical Ce–Fe bimetal oxides adsorbent: thermodynamics, kinetics and mechanism, Chem. Eng. J., 283 (2016) 721–729.
[41] Y. Guo, X. Xing, Y. Shang, B. Gao, L. Zhang, Q. Yue, Z. Wang, Multiple bimetallic (Al-La or Fe-La) hydroxides embedded in cellulose/graphene hybrids for uptake of fluoride with phosphate surroundings, J. Hazard. Mater., 379 (2019) 120634, doi: 10.1016/j.jhazmat.2019.05.027.
[42] S.S. Hosseini, A. Hamadi, R. Foroutan, S.J. Peighambardoust, B. Ramavandi, Decontamination of Cd^{2+} and Pb^{2+} from aqueous

solution using a magnetic nanocomposite of eggshell/starch/Fe_3O_4, J. Water Process Eng., 48 (2022) 102911, doi: 10.1016/j.jwpe.2022.102911.
[43] R. Foroutan, S.J. Peighambardoust, R. Mohammadi, S.H. Peighambardoust, B. Ramavandi, Development of new magnetic adsorbent of walnut shell ash/starch/Fe_3O_4 for effective copper ions removal: treatment of groundwater samples, Chemosphere, 296 (2022) 133978, doi: 10.1016/j.chemosphere.2022.133978.
[44] R. Foroutan, S.J. Peighambardoust, R. Mohammadi, S.H. Peighambardoust, B. Ramavandi, Cadmium ion removal from aqueous media using banana peel biochar/Fe_3O_4/ZIF-67, Environ. Res., 211 (2022) 113020, doi: 10.1016/j.envres.2022.113020.
[45] B. Liu, S. Lou, Y. Zeng, Y. Qin, W. Zhang, L. Zhang, X. Liu, High-efficiency adsorption of phosphate by Fe-Zr-La tri-metal oxide composite from aqueous media: performance and mechanism, Adv. Powder Technol., 32 (2021) 4587–4598.
[46] B.L. Wu, L.P. Fang, J.D. Fortner, X.H. Guan, I.M.C. Lo, Highly efficient and selective phosphate removal from wastewater by magnetically recoverable $La(OH)_3/Fe_3O_4$ nanocomposites, Water Res., 126 (2017) 179–188.
[47] C. Zhang, Y. Li, T.J. Wang, Y. Jiang, H. Wang, Adsorption of drinking water fluoride on a micron-sized magnetic Fe_3O_4@Fe-Ti composite adsorbent, Appl. Surf. Sci., 363 (2016) 507–515.
[48] Z. Wang, J. Su, X. Hu, A. Ali, Z. Wu, Isolation of biosynthetic crystals by microbially induced calcium carbonate precipitation and their utilization for fluoride removal from groundwater, J. Hazard. Mater., 406 (2021) 124748, doi: 10.1016/j.jhazmat.2020.124748.
[49] N. Chen, Z. Zhang, C. Feng, D. Zhu, Y. Yang, N. Sugiura, Preparation and characterization of porous granular ceramic containing dispersed aluminum and iron oxides as adsorbents for fluoride removal from aqueous solution, J. Hazard. Mater., 186 (2011) 863–868.
[50] J. Wang, N. Chen, M. Li, C. Feng, Efficient removal of fluoride using polypyrrole-modified biochar derived from slow pyrolysis of pomelo peel: sorption capacity and mechanism, J. Polym. Environ., 26 (2018) 1559–1572.
[51] J. Cheng, X. Meng, C. Jing, J. Hao, La^{3+}-modified activated alumina for fluoride removal from water, J. Hazard. Mater., 278 (2014) 343–349.
[52] X. Yu, S. Tong, M. Ge, J. Zuo, Removal of fluoride from drinking water by cellulose@hydroxyapatite nanocomposites, Carbohydr. Polym., 92 (2013) 269–275.
[53] T. Zhu, J. Gao, L. Zhang, W. Zhang, Enhanced adsorption of fluoride by cerium immobilized cross-linked chitosan composite, J. Fluorine Chem., 194 (2017) 80–88.
[54] F.C. Wu, R.L. Tseng, R.S. Juang, Enhanced abilities of highly swollen chitosan beads for color removal and tyrosinase immobilization, J. Hazard. Mater., 81 (2001) 167–177.
[55] A.I. Moral-Rodríguez, R. Leyva-Ramos, R. Ocampo-Pérez, J. Mendoza-Barron, I.N. Serratos-Alvarez, J.J. Salazar-Rabago, Removal of ronidazole and sulfamethoxazole from water solutions by adsorption on granular activated carbon: equilibrium and intraparticle diffusion mechanisms, Adsorption, 22 (2016) 89–103.
[56] C.E. Choong, M. Kim, S. Yoon, G. Lee, C.M. Park, Mesoporous La/Mg/Si-incorporated palm shell activated carbon for the highly efficient removal of aluminum and fluoride from water, J. Taiwan Inst. Chem. Eng., 93 (2018) 306–314.
[57] J. Lǔ, H. Liu, R. Liu, X. Zhao, L. Sun, J. Qu, Adsorptive removal of phosphate by a nanostructured Fe–Al–Mn trimetal oxide adsorbent, Powder Technol., 233 (2013) 146–154.
[58] A. Jeyaseelan, Mu. Naushad, T. Ahamad, N. Viswanathan, Design and development of amine functionalized iron-based metal organic frameworks for selective fluoride removal from water environment, J. Environ. Chem. Eng., 9 (2021) 104563, doi: 10.1016/j.jece.2020.104563.
[59] R.A.J.C. Ranasinghe, M.A.C.K. Hansima, K.G.N. Nanayakkara, Adsorptive removal of fluoride from water by chemically modified coal fly ash: synthesis, characterization, kinetics, and mechanisms, Groundwater Sustainable Dev., 16 (2022) 100699, doi: 10.1016/j.gsd.2021.100699.
[60] G. Murambasvina, C. Mahamadi, Effective fluoride adsorption using water hyacinth beads doped with hydrous oxides of aluminium and iron, Groundwater Sustainable Dev., 10 (2020) 100302, doi: 10.1016/j.gsd.2019.100302.
[61] D.R. Martinez-Vargas, E.R. Larios-Durán, L.F. Chazaro-Ruiz, J.R. Rangel-Mendez, Correlation between physicochemical and electrochemical properties of an activated carbon doped with lanthanum for fluoride electrosorption, Sep. Purif. Technol., 268 (2021) 118702.
[62] P.E. Díaz-Flores, J.A. Arcibar-Orozco, A.I. Flores-Rojas, J.R. Rangel-Méndez, Synthesis of a chitosan-zeolite composite modified with La(III): characterization and its application in the removal of fluoride from aqueous systems, Water Air Soil Pollut., 232 (2021) 235, doi: 10.1007/s11270-021-05185-1.
[63] Z. Wang, D. Shen, F. Shen, T. Li, Phosphate adsorption on lanthanum loaded biochar, Chemosphere, 150 (2016) 1–7.
[64] S.K. Milonjić, A consideration of the correct calculation of thermodynamic parameters of adsorption, J. Serb. Chem. Soc., 72 (2007) 1363–1367.
[65] Y. Gao, M. Li, Y. Ru, J. Fu, Fluoride removal from water by using micron zirconia/zeolite molecular sieve: characterization and mechanism, Groundwater Sustainable Dev., 13 (2021) 100567, doi: 10.1016/j.gsd.2021.100567.
[66] M. Nazari, R. Halladj, Adsorptive removal of fluoride ions from aqueous solution by using sonochemically synthesized nanomagnesia/alumina adsorbents: an experimental and modeling study, J. Taiwan Inst. Chem. Eng., 45 (2014) 2518–2525.
[67] B. Pan, J. Xu, B. Wu, Z. Li, X. Liu, Enhanced removal of fluoride by polystyrene anion exchanger supported hydrous zirconium oxide nanoparticles, Environ. Sci. Technol., 47 (2013) 9347–9354.